Decadal Background for Active Extreme Drought Episodes in the Decade of 2010–19 over Southeastern Mainland Asia🖉

Lin Wang,[a] Gang Huang,[b,c] Wen Chen,[b,d] Ting Wang,[c,e] Chakrit Chotamonsak,[f] and Atsamon Limsakul[g]

[a] *CAS Key Laboratory of Regional Climate-Environment for Temperate East Asia, Institute of Atmospheric Physics, Chinese Academy of Sciences, Beijing, China*
[b] *State Key Laboratory of Numerical Modeling for Atmospheric Sciences and Geophysical Fluid Dynamics, Institute of Atmospheric Physics, Chinese Academy of Sciences, Beijing, China*
[c] *University of Chinese Academy of Sciences, Beijing, China*
[d] *Center for Monsoon System Research, Institute of Atmospheric Physics, Chinese Academy of Sciences, Beijing, China*
[e] *Carbon Neutrality Research Center, Institute of Atmospheric Physics, Chinese Academy of Sciences, Beijing, China*
[f] *Department of Geography, Faculties of Social Sciences, Chiang Mai University, Chiang Mai, Thailand*
[g] *Environmental Research and Training Center, Pathum Thani, Thailand*

ABSTRACT: Severe and extreme drought in southeastern mainland Asia (SEMA) worsened drastically in 2010–19, occurring more than twice as frequently as in the preceding decade. It is found that the spring rainfall has undergone a concordant positive-to-negative transition with the turning point at 2010, and can explain 43% of the overall regime shift toward exaggerated severely dry condition. Associated with the decadal precipitation change, the anomalous northeasterlies prevail over SEMA, resulting in weakened eastward moisture propagation from the Indian Ocean as well as enhanced divergence. Meanwhile, there is downward motion over SEMA. This circulation pattern is remotely forced by a teleconnection from the tropical western Indian Ocean (TWI) SST. TWI SST is negatively correlated with SEMA precipitation and highlights a regime shift around 2010, after which the TWI has persistent warm SST helping to maintain deficient SEMA precipitation. In terms of the physical mechanism, the heating in the TWI warms the troposphere aloft and emanates wedge-shaped Kelvin waves with their northeast flank traversing SEMA, where friction-driven northeasterly low-level wind and divergence emerge to block moisture penetration from the Indian Ocean. The low-level divergence is followed by descending motion in SEMA, suppressing convection and rainfall. Further, the simulated structure forced by TWI SST alone bears a close resemblance to the observed evidence, confirming the critical role of the TWI. Finally, it is shown that ENSO and its diversity have a modulating effect on SEMA precipitation as well as on the coupling between TWI SST and SEMA precipitation, during both the previous winter and the concurrent spring.

SIGNIFICANCE STATEMENT: In the last decade, a sequence of extreme droughts has swept southeastern mainland Asia (SEMA), resulting in tremendous losses. Instead of examining individual extreme cases, this study aims to advance the understanding of how the active extreme drought episodes can be modulated by the decadal background and to reveal the underlying physical mechanisms. The results suggest that decadal change can explain 43% of the overall regime shift toward more extreme dry conditions, and that the sea surface temperature in the tropical west Indian Ocean has a profound impact. The knowledge obtained here has benefits for estimation of overall risks to extreme drought hazards and highlights the future work direction that skillful decadal prediction is crucial for robust planning in an uncertain climate.

---

1. Introduction

Southeastern mainland Asia (SEMA), including the southwestern parts of China, is one of the most populated regions in the world with rapid socioeconomic development, urbanization, and industrialization. The domain of SEMA in East Asia, spanning the region 10°–30°N, 95°–110°E, and its geographic features are portrayed in Fig. 1. It is necessary to stress that the study domain here is SEMA rather than Southeast Asia (SEA), which explicitly refers to the region comprising the 11 nations of Vietnam, Laos, Cambodia, Thailand, Myanmar, Malaysia, the Philippines, Indonesia, Brunei, Singapore, and Timor-Leste. SEMA has abundant surface water resources, as it is home to some major river systems including the Lancang–Mekong, Yangtze, Nujiang–Salween, Red, Irrawaddy, and Chao Phraya Rivers. Agriculture and livelihood in SEMA are heavily water dependent, which makes it highly susceptible to climate change and its variability. In particular, drought hazards and associated water crisis have already posed a serious challenge to agricultural production, food security, drinking water supply, ecosystems, and economies over SEMA.

In the recent decade, a sequence of extreme droughts has swept SEMA, resulting in tremendous losses. The northern
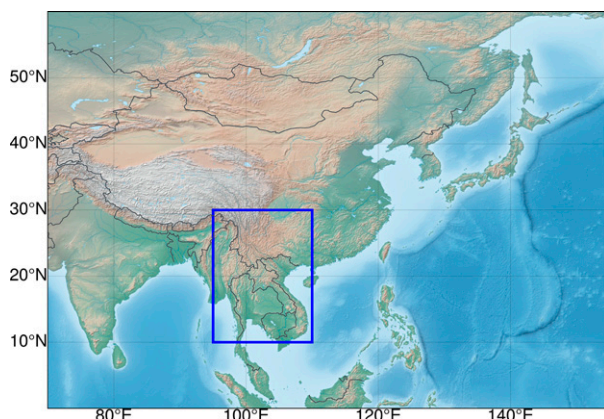
FIG. 1. Geographic features in East Asia and the location of the study domain SEMA (10°–30°N, 95°–110°E) outlined by the blue box.

part of SEMA [Southwest China (SWC)] has been frequently struck by exceptional and sustained droughts, with episodes in the summer of 2006, the autumn of 2009 to the spring of 2010, the summer of 2011, and late spring to early summer in 2019 being record-breaking events (Wang et al. 2015). All these droughts have resulted in tremendous losses, including crop failure, a lack of drinking water, ecosystem destruction, health problems, and even deaths. Taking the most recent drought period of April–June 2019, it is reported a total of 1.35 million hectares (ha) of crop including 79 000 ha of total crop failure and 6.562 billion yuan of direct economic loss (Ding and Gao 2020). Over the southern part of SEMA (the Indo-China Peninsula), the severity of two drought events during 2015–17 and 2018–20 exceed anything recorded in the past two decades (ESCAP 2019). For example, in Vietnam, 18 provinces were affected and 2 million people were in need of humanitarian assistance during 2015–17, and nearly 14 900 ha of crops were affected and nearly 138 800 regional households lacked water for daily use during 2018–20 (ReliefWeb 2017, 2020). In sum, these droughts have constituted devastating and far-reaching threats to multiple sectors of local lives, and thus have attracted great concern from both governments and the academic sector.

To date, considerable efforts have been made to explore the features and causes of droughts in SEMA. The contributions can be roughly categorized into two groups, one related to the individual extreme events in the recent decade and the other being long-term interannual or interdecadal variation. With regard to case studies, Barriopedro et al. (2012) report that the drought in Southwest China from summer 2009 to winter 2010 was triggered by weakened South Asian monsoon in summer and then maintained by extremely negative phases of the Arctic Oscillation (AO) in the ensuing winter. The role of the AO is also noted by Yang et al. (2012). In addition, Zhang et al. (2013) indicate that warm pool El Niño is also an important factor. Sun et al. (2019) suggest that the drought in June–October 2011 could be mainly attributed to lower rainfall, while the evaporation has comparable impact on the drought in 2010. In the Indo-China Peninsula, the record-breaking drought during 2015–16 is found to be associated with the synergy between anthropogenic warming and a strong El Niño (Christidis et al. 2018; Thirumalai et al. 2017). For the recent exceptional drought during March–June 2019 in southwestern China, S. Wang et al. (2021) illustrated that anthropogenic influence has increased the risk of dry extremes by 13%–23%. In addition to anthropogenic forcing, Ding and Gao (2020) indicated that the abnormally late onset of the rainy season is the direct reason as a consequence of weak southern branch trough and strong anticyclonic flow prevailing over the Bay of Bengal.

Besides case studies, other research has focused on long-term changes and related mechanisms over SEMA at multiple time scales. Zhang et al. (2021) evaluated the human influence on the increasing drought risk over Southeast Asian monsoon region based on CMIP6 ensembles, and identified the time of emergence of anthropogenic forcing that occurred in the 1960s. Park et al. (2020) found a dipole mode between southern China and Indo-China Peninsula for the boreal spring during 1979–2017, which is probably driven by ENSO and its associated anticyclonic anomaly over the South China Sea and the Philippines. Such a dipole mode is also observed in the early summer, as reported by Leung et al. (2020). However, they suggested that the remote influence originated from the tropical western Indian Ocean with the monsoon trough serving as a key bridge. In addition, Qian et al. (2020) investigated the persistence of such a dipole signal through spring to summer. It turns out that whether it persists or not is determined by the meridional position of the anomalous low-level anticyclone over the tropical western Pacific, which is jointly driven by the in situ SST anomalies and eastward atmospheric wave train across the Eurasian continent. As to the decadal shifts, Tan et al. (2017) found the sustained winter precipitation deficit in Southwest China after 2000, which was associated with decadal transition of AO toward its negative phases and frequent El Niño, especially the central Pacific El Niño. Wang et al. (2018) and Jia et al. (2021) both confirmed the wet-to-dry shift of autumn precipitation in Southwest China and the critical role of continuous warming in tropical warm pool. Recently, L. Wang et al. (2021) revealed two extreme drought hot spots in the last decade, with one located in SEMA. However, the preceding decade (2000–09) witnessed fairly mild conditions.

In addition, projecting the trends and severity levels of future droughts is another hot topic in SEMA, though not the concern of this study. Recently, Tangang et al. (2020) and Supari et al. (2020) projected future changes in climatological precipitation and the extremes over SEA, respectively. Other work has characterized the future scenario on a subregional scale, for example Southwest China (Wang and Chen 2014; Wang et al. 2014) and Vietnam (Nguyen-Ngoc-Bich et al. 2021).

Although many studies have been conducted with focus either on extreme cases or on long-term changes, the role of decadal background in active extreme drought episodes in the last decade is not well understood. What is the connection between decadal oscillation and the jump transition toward more extreme droughts in the last decade? What is the

quantitative contribution of decadal effects and the associated physical mechanisms? Motivated by the above knowledge gap, this study aims to unveil the decadal background for active extreme drought episodes in the last decade (2010–19) over SEMA. The paper is structured as follows. Section 2 describes the data and methods employed. The results are presented in section 3. Finally, a discussion and conclusions are provided in sections 4 and 5.

2. Data and methods

a. Data

Monthly gridded precipitation are retrieved from the latest version TS4.04 of Climatic Research Unit (Harris et al. 2020). The data are available at 0.5° × 0.5° horizontal resolution and extend over the global land. Given the relatively poor quality and low spatial density of in situ measurements in the earlier part of the twentieth century, the data records from 1960 onward are used. In addition, the ETOPO 1-arc-min gridded elevation data (Amante and Eakins 2009) and global land-cover map V2.3 (http://due.esrin.esa.int/page_globcover.php) are employed to exclude the high-elevation zones and barren land, where drought index computation is problematic.

To examine the atmospheric circulation patterns, this study uses Japanese 55-year Reanalysis (JRA-55) data compiled by the Japan Meteorological Agency. JRA-55 is the first comprehensive reanalysis that has covered the last half-century (Kobayashi et al. 2015). The striking features of JRA-55 production include the usage of the full observing system and the application of an advanced four-dimensional variational data assimilation scheme (Harada et al. 2016). JRA-55 spans 1958 to the present and has a horizontal resolution of 1.25° × 1.25° and 37 levels from 1 to 1000 hPa. The variables analyzed in this paper are vertically integrated moisture transport (kg m^{-1} s^{-1}), total precipitable water (kg m^{-2}), vertical velocity (Pa s^{-1}), geopotential height (gpm), and horizontal wind (m s^{-1}). Further, the Hadley Centre Sea Ice and Sea Surface Temperature dataset (HadISST; Rayner et al. 2003) is used to analyze the atmospheric teleconnection patterns associated SST anomalies. The HadISST is released on a 1° latitude–longitude grid from 1870 to the present.

For all data, we adopted the common period from 1960 to 2019 with focus on the recent two decades.

b. Methods

1) STANDARDIZED PRECIPITATION INDEX

The popular drought index SPI (Standardized Precipitation Index), first developed by McKee et al. (1993), is used here for estimating wet or dry conditions based on precipitation amount alone. The SPI is essentially a probability-based index, which expresses the actual rainfall as a standardized departure with respect to probability distribution function (Hayes et al. 2011). The calculation steps comprise fitting the cumulative precipitation over predefined duration to a proper parametric distribution, transforming probability distribution into a standard normal distribution, and finally computing the

inverse probability to obtain the index (Edwards and McKee 1997). The full calculation step by step is elaborated in text S1 in the online supplemental material. A negative SPI indicates dryness and more negative values mean more intense and rarer drought. In the SPI calculations, we adopted a two-parameter gamma distribution, a 40-yr reference period of 1960–99, and a time scale of 12 months.

Here we would like to explain why SPI is used instead of Standardized Precipitation Evapotranspiration Index (SPEI; Vicente-Serrano et al. 2010), which is regarded as a more comprehensive measure of water availability with evaporative demand involved. On the one hand, this study aims to investigate the precipitation-induced drought. On the other hand, L. Wang et al. (2021) have recently reported that the extreme drought episodes over SEMA in the recent decade are mainly promoted by precipitation anomalies whose contributions are generally larger than 80%. As such, SPI best meets our needs.

2) STATISTICAL DIAGNOSES

The regular statistical methods used include composite analysis, correlation analysis, linear regression analysis, and Student's t test. These are classic methods and will not be described in detail here.

To obtain modes on the scale of decades, a low-pass Butterworth filter with a 10-yr cutoff and empirical mode decomposition (EMD) are used. The basic principle and frequency response of low-pass Butterworth filter are presented in text S2 and Fig. S1 in the online supplemental material. Compared to another popular filtering technique called Lanczos filtering, there is no loss of data at the beginning and end of the series to which the Butterworth filter is applied. To test the sensitivity of the resultant low-frequency changes to the methods, the complementary Lanczos filter is also applied. In parallel, we take advantage of the Complete Ensemble Empirical Mode Decomposition with Adaptive Noise (CEEMDAN) method developed by Torres et al. (2011), which is an improved method of classic EMD. For simplicity, the term EMD is used to refer to CEEMDAN in this study.

To separate the internal variability of SST from the external forcing mainly due to global warming, the globally forced signal is approximated at each grid point by the regression of the SST anomaly on the global mean SST anomaly (Frankignoul et al. 2017). The estimated forced signal has spatially nonuniform amplitude. To get rid of the impacts due to ENSO or other high-frequency variability, the global mean SST has been presmoothed by a binomial (1/4–1/2–1/4) filter. Then, the internally generated variations are inferred by subtracting the forced SST signal from the observations at each grid cell. To further assess the robustness of the result, an alternative approach to remove the forced signal by removing the CMIP6 ensemble mean is carried out, which is detailed in text S3 in the online supplemental material.

3) LINEAR BAROCLINIC MODEL

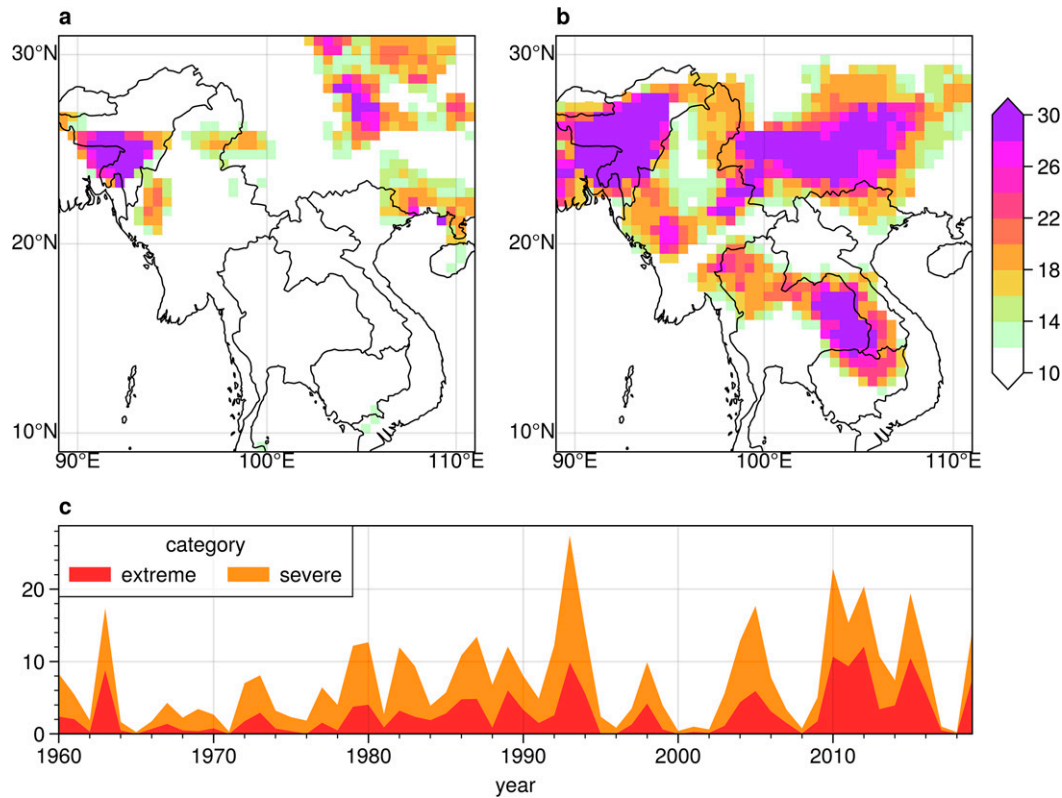To understand the mechanisms linking SST, circulation, and rainfall, a moist version of a linear baroclinic model

Fig. 2. (a),(b) Spatial pattern of the number of drought months under severe drought (SPI < -1.5) in the periods of 2000–09 and 2010–19. (c) Temporal evolution of percentage area (%) under extreme (red) and severe (orange) drought categories over SEMA.

(LBM) is devised to examine a steady linear response to prescribed forcing (Watanabe 2003). Compared to a fully nonlinear AGCM, it facilitates an interpretation of complicated feedback by removing nonlinearity in the dynamical atmosphere. Meanwhile, the LBM requires lower computational cost. The moist LBM includes moist diabatic processes, enabling us to solve a steady-state response of the coupled dynamical–convective system to a given SST anomaly (Watanabe and Jin 2003).

For this work, the moist LBM is configured with a spectral T42 horizontal resolution and 20 vertical levels. The basic state is derived from the spring (March–May) mean climatology of the NCEP reanalysis data during 1958–97. In parallel, mean fields for SST and ground wetness are also set up. The moist LBM experiment is forced by an idealized SST anomalies specified over the desired sector and integrated for 30 days, with the last 20-day average being approximated as the steady solution. Finally, we would like to explain why we use NCEP rather than JRA-55 data to make basic states as required in the LBM simulation. It is because the NCEP climatological month mean data bundled in the LBM release have been formatted and can be readily read by the model program. As reflected in Fig. S2, which compares the JRA-55 and NCEP reanalysis data for the four necessary variables required by LBM, the overall agreement between the two reanalysis datasets justifies the use of the NCEP-based climatological field.

3. Results

a. Decadal shift to more frequent severe and extreme droughts

In this section, the occurrence frequencies and spatial extent of severe and extreme droughts over SEMA are explored. Here, we define SPI values less than -1.5 and -2 representing severe and extreme drought classes, respectively. Note that extreme category is totally the subset of severe category. Figures 2a and 2b illustrate the spatial distribution of number of drought months under severe drought in the periods of 2000–09 and 2010–19. Similar outcomes are found for the extreme drought category but to a lesser degree, so the redundant pictures are not shown.

During 2000–09, SEMA is less exposed to severe droughts with 77% of the grids over SEMA receiving no more than 10 months of severe drought, as seen in Fig. 2a. The regional average frequency is 6.6 months decade^{-1} and in particular there are 20% area never experiencing severe drought. However, in the subsequent decade of 2010–19, severe drought conditions in the SEMA had deteriorated drastically with prominent centers formed in Southwest China, east of Thailand, and parts of Myanmar, as indicated by Fig. 2b. Specifically, the regional average frequency has jumped to 14.7 months decade^{-1}, more than twice as frequently in the preceding decade, and the area affected by severe drought for more than 10 months
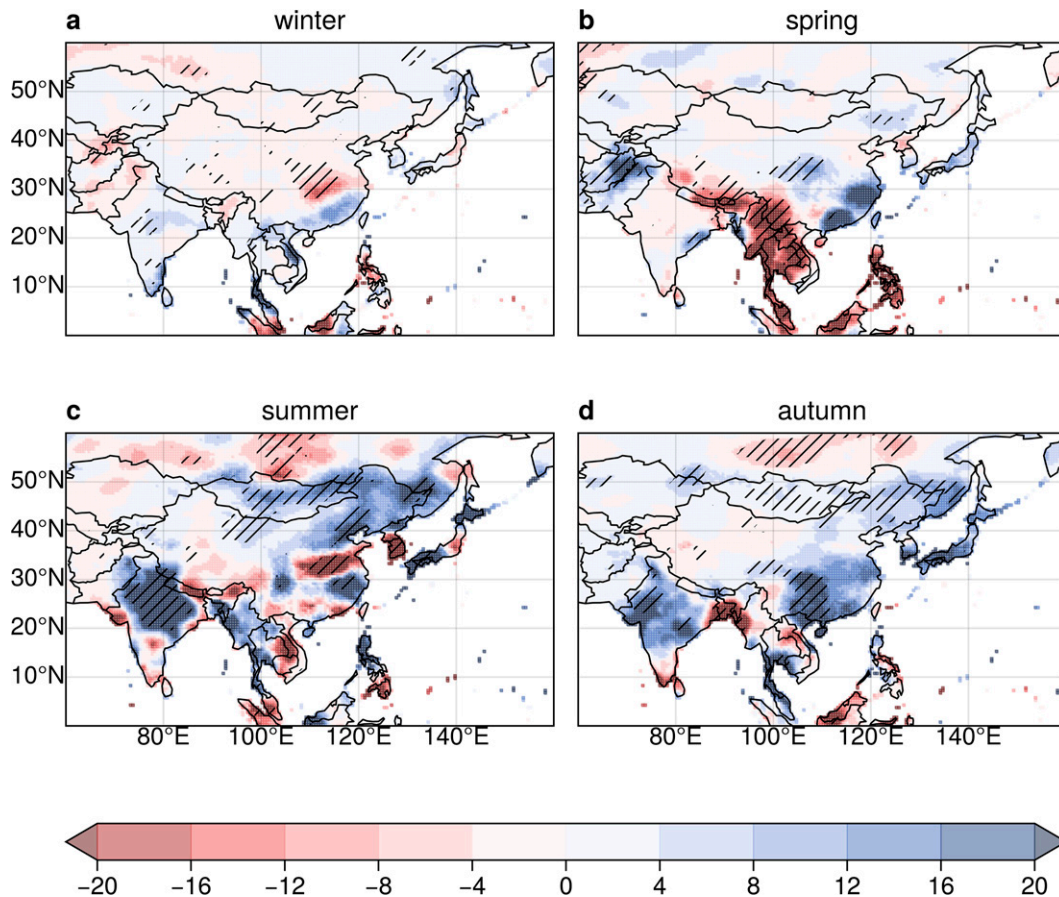
FIG. 3. The precipitation changes between 2010–19 and 2000–09 for (a) winter, (b) spring, (c) summer, and (d) autumn, with statistically significant differences at 0.1 significance level hatched.

occupies 65% of the total. In addition, the severe droughts have spread into almost the whole SEMA region, with the undisturbed area having shrunk to 10%.

Figure 2c portrays the temporal evolution of spatial coverage of severe and extreme droughts throughout the entire period. Significant increase in both drought categories can be detected from 2000–09 to 2010–19. In detail, the extreme drought coverage is subjected to a remarkable increase from 1.84% to 6.39% and the severe drought coverage has been doubled from 5.5% to 12.26%, thus again evidencing a shift toward heavier droughts period. Particularly, the 2010–19 episode is also identified as the period with the highest extent hit by severe or extreme droughts. In the recent 20-yr period, severe and extreme droughts were mainly witnessed in the year 2005, 2010, 2011, 2012, 2015, 2016, and 2019, with most recorded in the recent decade.

In above survey, it is found that the severe and extreme droughts exhibit an interdecadal change approximately around 2010, after which SEMA tends to become drier. To determine which season's precipitation is most responsible for the interdecadal change of severe and extreme drought in SEMA, the average seasonal changes in precipitation between 2010–19 and 2000–09 along with statistical level are estimated. Comparing patterns in the four seasons in Fig. 3,

spring precipitation over SEMA stands out to receive notably less precipitation in the recent decade compared to the preceding one. The negative precipitation anomalies amount to −14.6 mm on average, and statistically significant declines dominate most parts of SEMA. In contrast, such interdecadal signals in spring precipitation are not noticed in other seasons. In short, accompanying the above described severe and extreme drought changes, it is spring precipitation that has undergone a concordant decadal shift.

Apart from the spatial pattern, Fig. 4 is displays the raw and 10-yr low-pass filtered time series averaged over SEMA in four seasons from 1960 to 2019. Here, the decadal component is extracted by performing a Butterworth filter, but the result is consistent with that obtained by the Lanczos filter as shown in Fig. S3. Regarding the spring season, the presence of a decadal cycle rather than a trend is characteristic of rainfall in SEMA, as the trend slope and associated *p* value are near-zero and 0.5, respectively. To be more specific, there is a clear alternate regime of above and below normal rainfall in the former and the latter decade of the 2000–19, with the turning point locked at 2010. This interdecadal fluctuation is well consistent with the strengthening of severe and extreme droughts from 2000–09 to 2010–19. In the remaining seasons, however, the opposite behavior is observed in respect to the
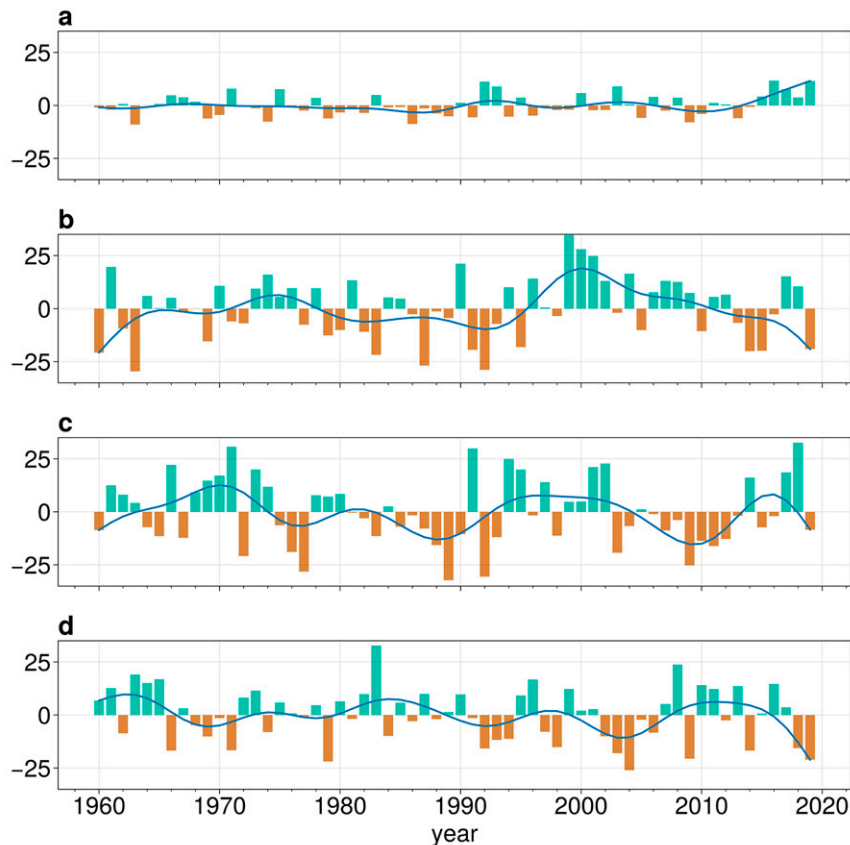
FIG. 4. Raw (bars) and 10-yr low-pass filtered (curves) time series of seasonal precipitation anomalies in (a) winter, (b) spring, (c) summer, and (d) autumn from 1960 to 2019.

drought variability. In conclusion, the spring precipitation over SEMA plays a crucial role in modulating the severe and extreme drought tendency on a decadal time scale in the most recent 20 years. Finally, we would like to stress that the result does not deny the nonmarginal influence of interannual variability (e.g., the obvious rainfall deficits that occurred in the summers of 2012 and 2019 and autumns of 2014, 2018, and 2019), but the goal of the present work is dealing with the decadal background.

In what follows, the quantitative contribution of spring precipitation is estimated. To this end, the SPI values are recalculated by holding the spring precipitation in the period of 2000–19 as its climatology, and then the difference between the raw and the recalculated values denotes the effect due to spring precipitation variation. Figures 5 and 6 compare the severe and extreme drought frequencies with and without spring precipitation anomalies, in spatial and integrated perspective, respectively. In the absence of spring precipitation impact, a widespread reduction in severe and extreme drought incidence is noteworthy over SEMA, which is particularly pronounced in the Indo-China Peninsula. The average frequency of severe drought is reduced from 14.7 to 9.2 months (37.4% decrease) and that of extreme drought counterpart from 7.7 to 4.0 months (48% decrease). With a simple

arithmetic average, the decadal oscillation of spring precipitation can explain 43% of the observed drought tensions in the recent decade.

Figure 6 exhibits the percentage area for each bin of drought counts, depending on whether spring precipitation is included or not. A threshold value of 10 months is chosen to separate high and low burdens exerted by severe or extreme drought. For the severe drought category, the removal of spring precipitation contribution caused the high burden area to contract from 69% to 42% with a concurrent expansion of the light burden area by 27%. This is also the case for the extreme drought grade, albeit with a smaller percentage change of 23%.

Based on the above investigations, the decadal transition of spring precipitation is proved to be a critical driver of the enhanced extreme dry conditions in the recent decade. Therefore in the following section we will analyze the physical mechanisms from the aspects of atmospheric circulation and SST anomalies patterns related to the decadal transition.

b. Atmospheric circulation and SST anomalies patterns responsible

Before diving into the anomalous circulation and SST pattern, we briefly describe the climatological features related to
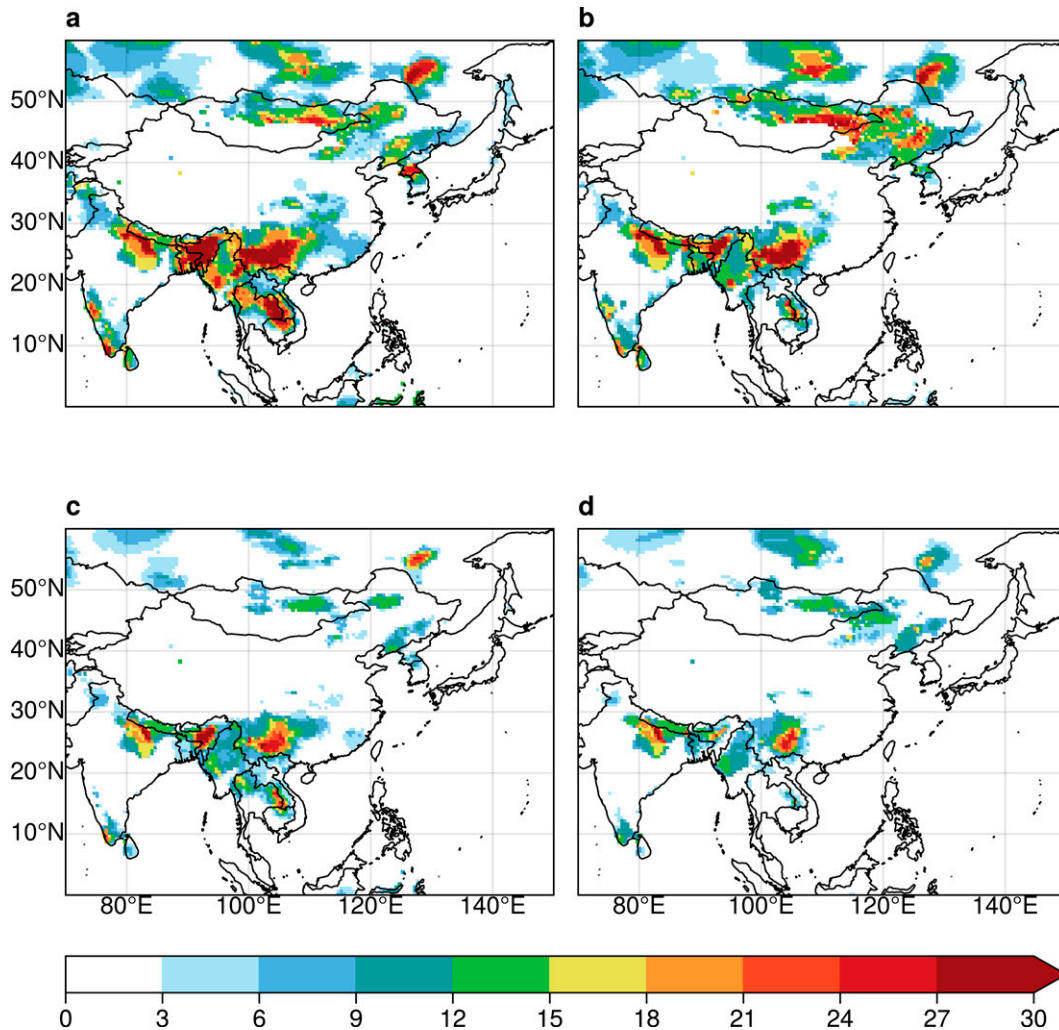
FIG. 5. (a),(b) Spatial pattern of the number of drought months under severe drought (SPI < -1.5) in the last decade (2010–19) for (a) raw precipitation data and (b) data with spring precipitation replaced by climatological values. (c),(d) As in (a) and (b), but for the extreme drought category (SPI < -2).

SEMA. Figures 7a and 7b show the geographic distribution of climatological spring precipitation over SEMA in the context of East Asia, and its corresponding portions of the annual cycle. Over the whole domain, the regions of highest rainfall (exceeding 200 mm) are situated in southern China, the Maritime Continent, and Bangladesh, as shown in Fig. 7a. In comparative terms, the SEMA receives moderate amounts rainfall of 93.4 mm on average, with more precipitation falling in the southern part than in the northern part. As regards annual cycle and interannual variability (Fig. 7b), rainfall is more abundant in summer, but the maximum 10th–90th percentile spread of about 86 mm is seen in May. That is, the rainfall in spring exhibits high variability despite the lower average amount.

Since moisture and lift are the two critical ingredients for producing precipitation, Figs. 7c and 7d display the climatological distribution of column moisture flux and vertical velocity at 500 hPa. The precipitation in SEMA is controlled by southwesterly moisture transport from the Indian Ocean and easterly transport from the Pacific Ocean. Given that the two conveyors collide mainly in the southern part of SEMA, strong convergence and rising motion occur there. In comparison, the northern part of SEMA is characterized by less obvious convergence and somewhat climatological downward motions. As a result, the climatological precipitation within SEMA follows a south–north gradient.

The following will discuss the anomalous condition, which is the main purpose here. Figures 8 and 9 together show the composite difference between 2000–09 and 2010–19 for vertically integrated moisture flux and its associated divergence, column precipitable water, streamfunction at 850 hPa, vertical velocity at 500 hPa, divergent wind and divergence at 200 hPa, and a height–horizontal cross section of flow vectors along the path from 0°, 60°E to 15°N, 110°E. In addition to the
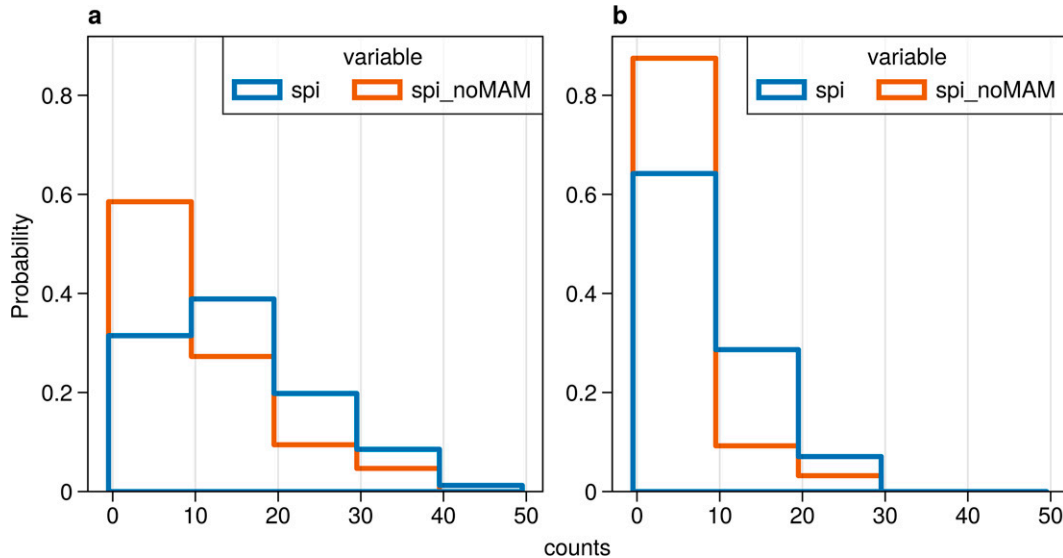
FIG. 6. Percentage area of (a) severe and (b) extreme drought counts over SEMA in the recent decade (2010–19). The blue and orange steps denote the quantities calculated based on raw data and on data with spring precipitation replaced by climatological values, respectively.

composite difference, the composite maps of moisture flux and precipitable water for the respective decade are also presented.

Since the composite circulation anomalies show clear symmetric structures between 2000–09 and 2010–19, we describe mainly the composite patterns tied to the dry decade of 2010–19. As shown in Fig. 8c, it can be seen that the anomalous easterlies prevail north of the equator of the Indian Ocean, indicative of weakened eastward propagation of water vapor. Meanwhile, the atmospheric circulation over SEMA is characterized by strong northeasterlies, which tend to prevent moisture penetration into the continent. The northeasterly seems to be part of an anticyclone developing over the Bay of Bengal (BOB), as reflected by the positive streamfunction anomalies at 850 hPa (Fig. 9a). However, the anomalous flow along the northern curvature is quite weak and less significant. On the whole, the mainstream belt stretches from SEMA to the east coast of Africa, which starts to follow a southwestward direction over SEMA, then turns westward after reaching the equatorial Indian Ocean, and finally converges to the east coast of Africa. As a consequence, the moisture transport from the tropical Indian Ocean to SEMA is blocked, with abundant moisture retained over the oceanic region but strong precipitable water reduction and moisture divergence identified over SEMA, as shown in Fig. 8f. In addition to Indian Ocean sector, there appears to be an anticyclone over the tropical northwest Pacific region, but its influence is more confined to Southeast China and the Maritime Continent rather than SEMA. Therefore, the anomalous circulation pattern with moisture over the Indian Ocean has played a crucial role in the last 10 years.

In subsequent analysis, the vertical circulation will be explored based on vertical velocity at 500 hPa and divergent wind at 200 hPa. As shown in Figs. 9b and 9c, there is anomalous ascent and upper-level divergence over the tropical western Indian Ocean, with one branch of the outflow heading northeastward and converging aloft over SEMA. As a result, local compensating subsidence prevails over SEMA and prevents the formation of convection and rainfall. Furthermore, the height–horizontal cross section of flow vectors along the path from 0°, 60°E to 15°N, 110°E is depicted in Fig. 9d. We choose this path to plot the overturning circulation as it corresponds well to the upper-level divergence and convergence centers. It clearly exhibits a vertical circulation cell, comprising ascending motions above TWI extending into about 200 hPa, divergent airflow moving toward SEMA in the upper atmosphere, and compensating subsidence occurring between 90° and 100°E. Hence, the downward branch over SEMA tends to suppress convection over SEMA and thus favors dryness.

Based on above analysis, it is speculated that a key remote factor is SST variation in the tropical western Indian Ocean (TWI). To substantiate the TWI–SEMA teleconnection, Fig. 10 shows the decadal behavior of TWI SST and its statistical relation with SEMA precipitation. Note that the warming signal in SST has been removed by subtracting a linear regression on the global mean SST. As shown in Figs. 10a and 10b, a significant negative-to-positive shift of internally generated SST variability is detected in TWI during the recent 20 years. The result is consistent with the that obtained by removing the CMIP6 ensemble mean, as shown in Fig. S4. Further, the EMD is applied to the raw TWI SST series to extract the secular trend and decadal variability, as represented by the fourth and third intrinsic modes, respectively. The high-frequency component first and second modes, although not the concern of this study, are shown in Fig. S5.
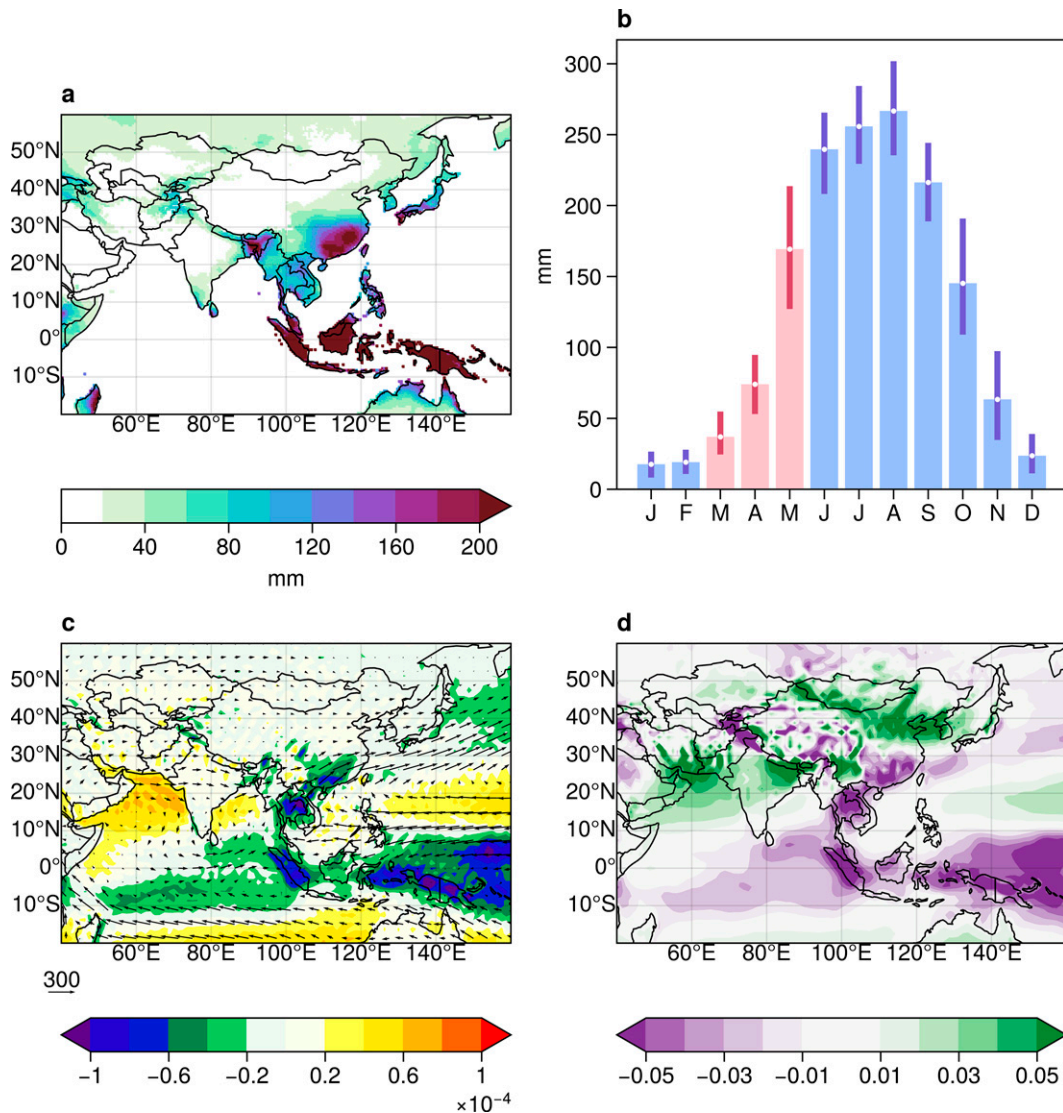
FIG. 7. (a),(c),(d) The climatological distribution of precipitation, divergence, and vertical velocity at 500 hPa, respectively. Also shown in (c) is vertically integrated moisture flux (vectors). (b) The annual cycle of precipitation averaged over the SEMA domain (10°–30°N, 95°–110°E) as outlined in Fig. 1.

As indicated by the secular mode in Fig. 10c, it is not surprising to find that the long-term change of TWI SST, which has risen by about 1°C, is evolving in parallel with the global anthropogenic warming. Rather than the long-term tendency, our primary concern is the decadal mode, which highlights a regime shift around 2010 as the most prominent during the whole period. In contrast, the period before twenty-first century is characterized by weak decadal oscillation. After 2000, decadal SST exhibits unprecedented large-amplitude oscillations with peak-to-peak difference of about 0.4°C. Comparing the decadal-scale TWI SST (line) and SEMA precipitation (bars) in Fig. 10d, a clear out-of-phase relation between the two appears to be most pronounced after 2000, which suggest that increased (reduced) precipitation occurs in SEMA during the negative (positive) phase of the TWI SST. Most

importantly, the phase shift of TWI SST exactly concurs with the timing of precipitation shift over SEMA, which is able to explain the wet-to-dry shift in SEMA. The coupling between TWI SST and SEMA precipitation along with the conditional modulation by ENSO will be further discussed in section 4.

Next, the dynamic process relating TWI SST to SEMA precipitation will be explored. The fundamental theory used here is the atmospheric Kelvin wave response to the anomalous heating in Indian Ocean, as proposed by Wu et al. (2009) and Xie et al. (2009). To this end, the tropospheric temperature averaged between 850 and 200 hPa, vertical velocity at 500 hPa, and column integrated moisture flux are regressed onto the normalized TWI SST, as illustrated in Fig. 11. The TWI surface warming significantly warms the troposphere through moist adiabatic adjustment, with one standard deviation
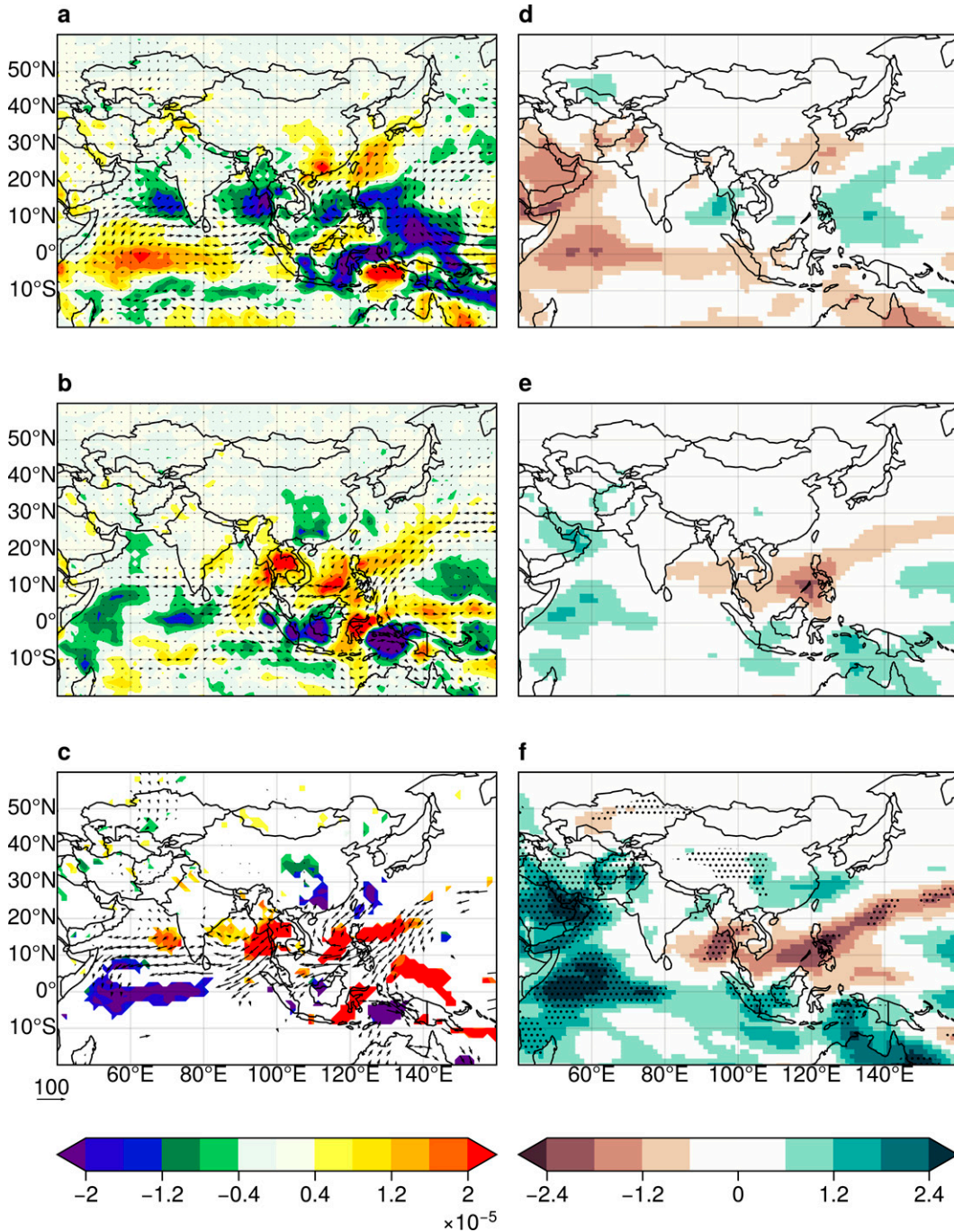
FIG. 8. Composite map for periods of (top) 2000–09 and (middle) 2010–19, and (bottom) their difference. (left) The vertically integrated moisture flux (vectors) and its associated divergence (shaded) composites and (right) the column precipitable water composites. For the difference field, only values significant at the 90% confidence level are plotted or stippled.

increase in TWI SST leading to a 0.06°–1°C increase of 850–200-hPa layer temperature. Subsequently, enhanced heating in the mid- to upper troposphere emanates a warm Kelvin wave into the Maritime Continent, accompanied by anomalous easterlies. Driven by low-level Ekman divergence

due to friction, northeasterly surface wind anomalies are found on the northeast flank of the Kelvin wave, causing moisture transport failure and divergence there. The resultant divergence further triggers suppressed convection and anomalous anticyclone over the BOB. The regressed values of moisture
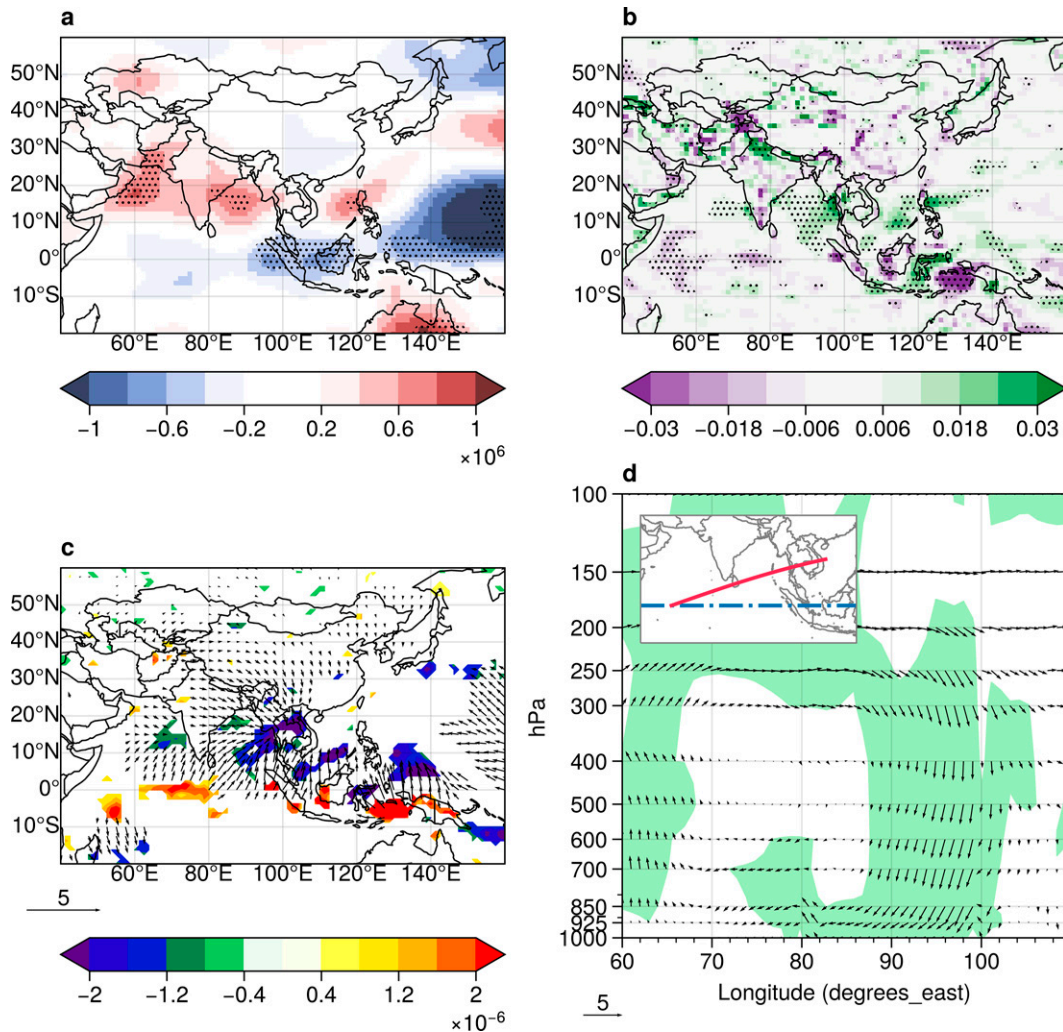
FIG. 9. Composite difference between 2000–09 and 2010–19 for (a) streamfunction at 850 hPa, (b) vertical velocity at 500 hPa, (c) divergent wind and divergence at 200 hPa, and (d) height horizontal cross section of flow vectors along the path from 0°, 60°E to 15°N, 110°E. The stippling in (a) and (b) and shading in (d) denote anomalies that are statistically significant at the 10% level, while in (c) only statistically significant values are drawn. The inset map in (d) shows the path of the cross section (red line) with the equator marked by blue dot–dashed line. The vertical velocity in (d) is multiplied by 100.

flux anomalies are estimated to be about 30 kg m^{-1} s^{-1}. Compared to the classic basin-scale warming in Indian Ocean, the TWI warming induced Kelvin wave wedge is much shorter in longitudinal extent, which can hardly penetrate into western Pacific. This hints that the broad-scale anticyclone over the northwestern Pacific is probably not the product of imposed TWI forcing, but is ENSO generated. Apart from the tropospheric temperature and horizontal circulation response, the shadings in Fig. 11 illuminate the vertical motion. We find the expected upward motion associated with the TWI heating. On the north side of equator, compensating sinking belt are present between 5° and 15°N.

In sum, the heating-induced Kelvin wave accompanied by northwesterly and vertical compensating circulation jointly couples the TWI SST and SEMA precipitation.

c. Numerical experiment

The above statistical diagnoses demonstrate that the remote influence originating from TWI SST may drive the SEMA precipitation. However, it is essential to verify the statistically derived connection between TWI SST and SEMA precipitation and to isolate the atmospheric response promoted by TWI SST alone. For this purpose, the LBM numerical experiment is launched with an idealized elliptical patch of positive SST anomalies imposed on spring SST climatology. The idealized SST forcing is prescribed to have a maximum value of +1.2°C at the center and gradually decrease to zero outward in both zonal and meridional directions, as illustrated in Fig. 12a. This provides a buffer zone to avoid numerical instability and spatial fragmentation. The averaged SST
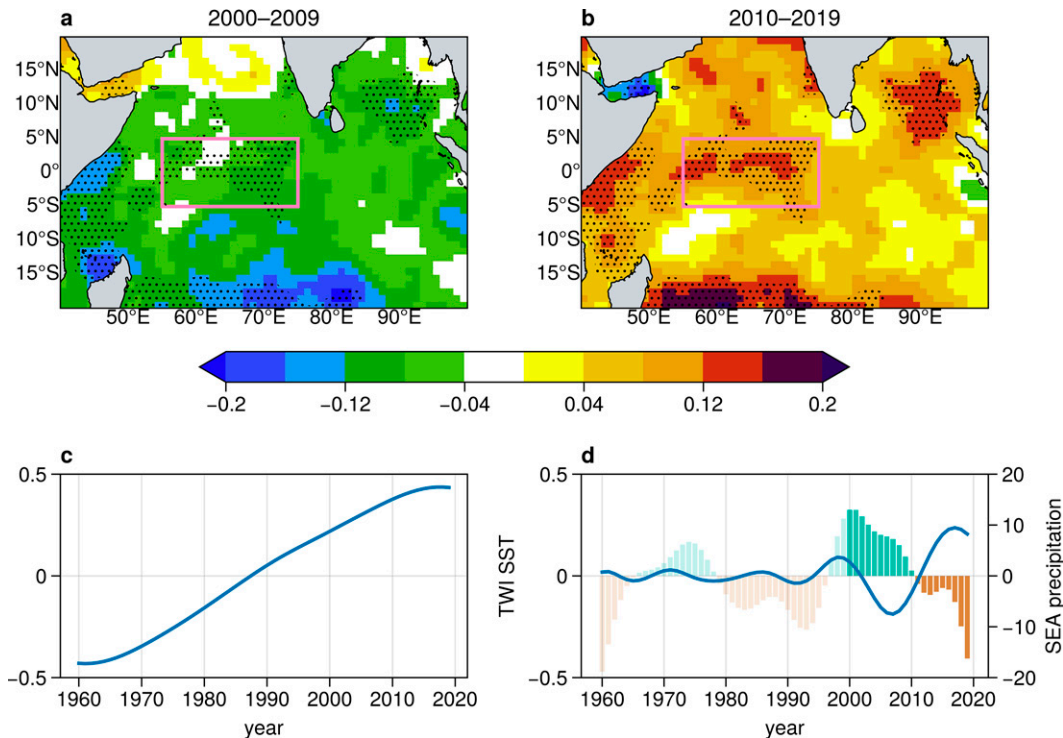
FIG. 10. (a),(b) The composite of internal SST variability in 2000–09 and 2010–19. (c),(d) The fourth and third EMD modes (lines) of SST over TWI, with decadal precipitation over SEMA (bars) overlaid.

anomaly over TWI is 0.4°C, in line with the observed peak-to-peak decadal discrepancy (Fig. 10d).

Figures 12b–e show the responses of 850–200-hPa temperature, vertical velocity at 700 hPa, and wind vectors and
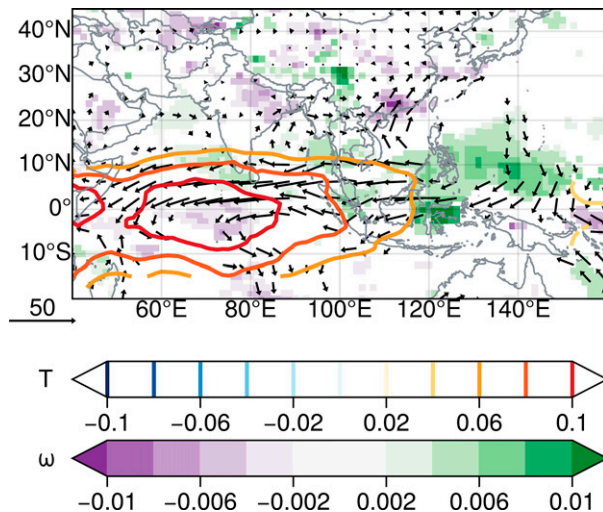

FIG. 11. Regression of normalized TWI SST onto tropospheric temperature averaged between 850 and 200 hPa with the global warming signal removed (contours), vertically integrated moisture flux (vectors), and vertical velocity at 500 hPa (shaded). Only statistically significant values are drawn.

divergence at 500 and 900 hPa. As a result of the warmer SST, the 850–200-hPa averaged temperature is about 0.2–0.4 K warmer than the benchmark state. Figure 12b also indicates that the tropospheric warming displays a Kelvin wave extending into the Maritime Continent, which is wedge-shaped and symmetric about the equator. The simulated temperature distribution is generally consistent with the observation-based regression pattern (Fig. 11).

In terms of vertical motion, increasing SST over the TWI region increases local vertical ascending motion due to the stronger convection, with a compensating subsidence appearing on both southern and northern flanks of about 10°–20° off the equator (Fig. 12c). The northern subsidence belt obviously covers the whole SEMA, although not where the response is greatest. Therefore, the convective activity and precipitation over SEMA is expected to be suppressed. In terms of horizontal dimension, Figs. 12d and 12e show the wind vectors along with divergence anomalies at 500 and 900 hPa, respectively. At free atmosphere, it can be seen that the easterly wind anomalies, caused by the warm Kelvin wave, traverse the entire tropical Indian Ocean (Fig. 12d). However, we are more interested in the low-level circulation features, which are fundamental for the moisture supply. As shown in Fig. 12e, a strong northeasterly wind blows in SEMA along with strong divergence there, weakening the moisture penetration and convergence over SEMA. Such local circulation features over SEMA as simulated by LBM closely resemble the observed composite as
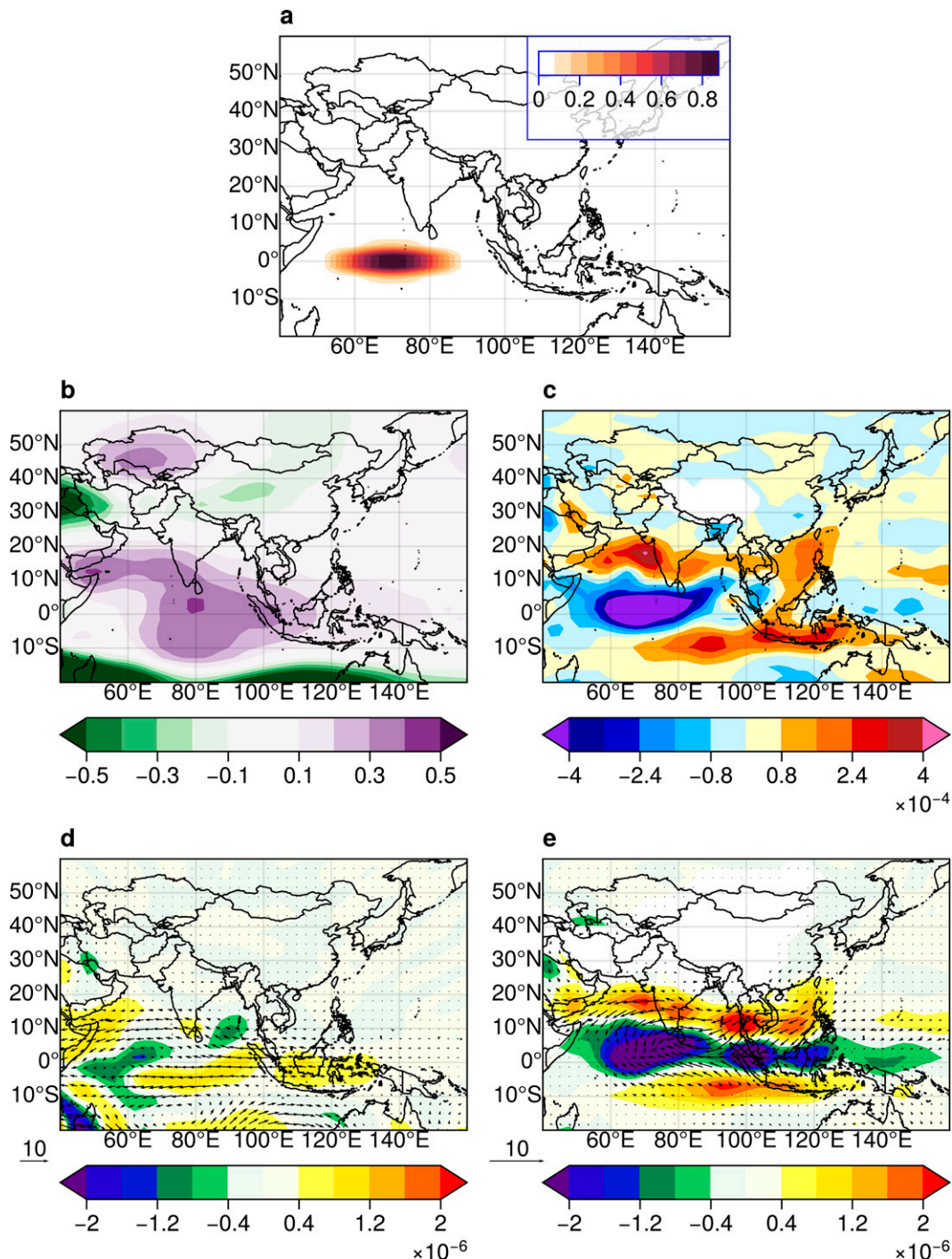
FIG. 12. (a) SST anomaly patterns specified in the modeling experiments (units: K). (b)–(e) The response of 850–200-hPa temperature (unit: K), vertical velocity at 700 hPa (unit: hPa s^{-1}), wind vectors, and divergence at 500 and 900 hPa (unit: m s^{-1}).

well as the regression pattern (Figs. 8 and 11). Besides, the broad-scale pattern is also well reproduced by the experiment with SST forcing in TWI alone—for example, the easterlies along 10°N, the anticyclonic flow over the BOB, and the convergence over the equator between 60° and 80°E. In

addition, the warm TWI SST also leads to an anticyclone over northwestern Pacific, but the degree of abnormality is far too much weaker. This supports the statistical inference made above that the anticyclone over northwestern Pacific is more ENSO-regulated.
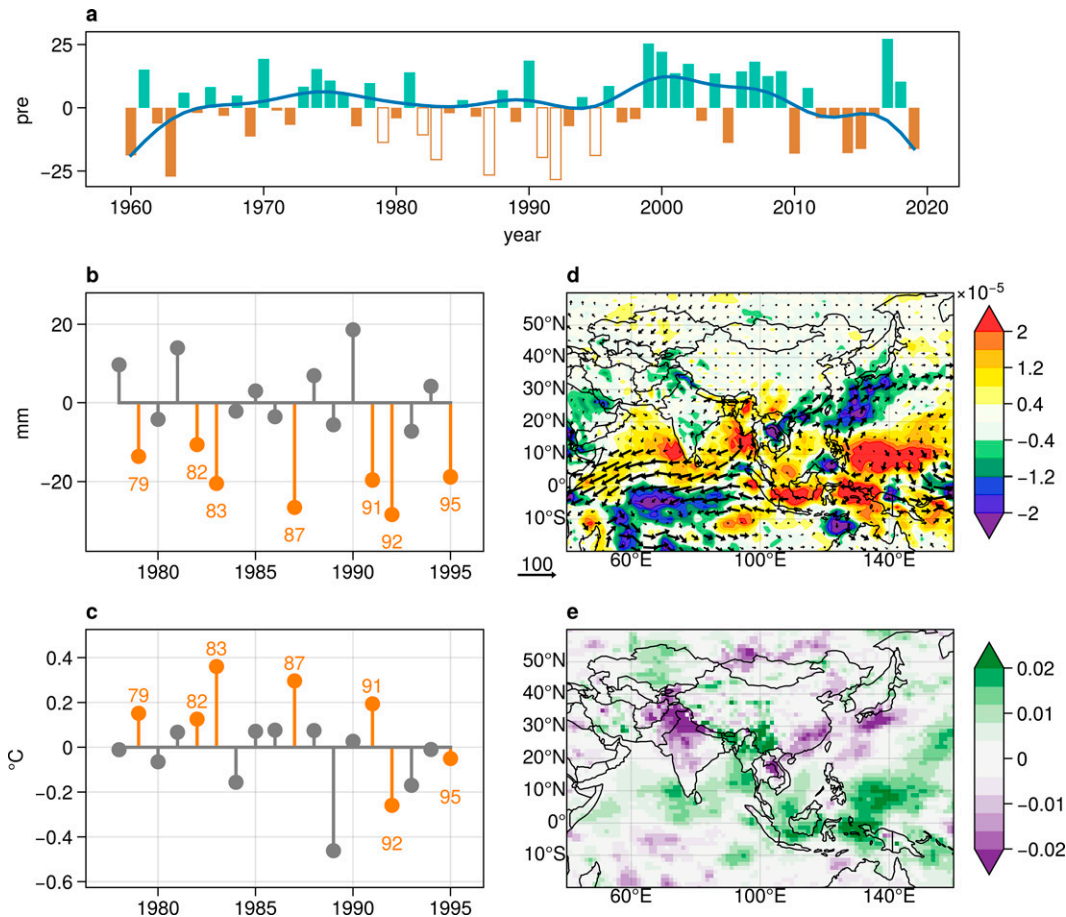
FIG. 13. (a) As in Fig. 4b, but the low-pass filter is applied to the time series with the seven outlier years (1979, 1982, 1983, 1987, 1991, 1992, and 1995) removed. (b),(c) The temporal evolution of SEMA precipitation and TWI SST during 1978–95. (d),(e) The composite anomalous pattern of vertically integrated water flux along with divergence and vertical velocity at 500 hPa.

In conclusion, the teleconnected influence of TWI SST on SEMA precipitation is likely to be physical, rather than just statistical.

4. Discussion

In this section, we further examine the coupling between SEMA precipitation and TWI SST, and the modulating role of ENSO is also explored. Most of our analysis above is restricted to the decadal shift from 2000 onward, but another decadal change of decreased spring rainfall over SEMA can also be observed during 1978–95, as shown in Fig. 4b. This raises the obvious question whether the long-lasting precipitation deficits during 1978 to 1995 is triggered by warm TWI SST as well. First, it is found that that the dry period is to some extent the consequence of some very dry outlier years that occurred in 1979, 1982, 1983, 1987, 1991, 1992, and 1995. As indicated by Fig. 13a, if the seven outlier years are removed, the decadal dryness almost disappears. Among the driest years, there are five out of seven cases that exhibit significant above-normal TWI SST, and the precipitation

response is found to be approximately proportional to the magnitude of TWI SST anomalies, by a visual comparison of Figs. 13b and 13c. Furthermore, the composite patterns of moisture flux and vertical velocity, as shown in Figs. 13d and 13e, tend to closely resemble not only the modeled forced pattern arising from warm TWI SST, but also the decadal time scale climate anomalies in the recent decade. The result is convincing that the TWI SST does have profound impacts on the decadal precipitation deficits during 1978–95. Nevertheless, an important difference is highlighted that the northeasterlies over SEMA is westward-located (Fig. 13d) compared to those in the recent decade (Fig. 8c), with the east fringe of SEMA instead governed by southwesterlies as a part of the anticyclone. In the following, we show the coupling between TWI SST and SEMA precipitation probably modulated by ENSO.

To investigate the effect of ENSO and its diversity, the Niño-3.4 index, the Niño-3 index, and the El Niño Modoki index (EMI) are constructed to represent the ENSO, eastern Pacific (EP) ENSO and central Pacific (CP) ENSO (e.g., Feng et al. 2011; Ma et al. 2020). The Niño-3.4 index is the averaged

SST anomaly over 5°S–5°N, 170°–120°W, while the Niño-3 index is that over 5°S–5°N, 170°–120°W. The EMI index is built following Ashok et al. (2007):

$$EMI = [SSTA]_A - 0.5 \times [SSTA]_B - 0.5 \times [SSTA]_C,$$

where the brackets indicate averaging in region A (10°S–10°N, 165°–140°W), region B (15°S–5°N, 110°–70°W), and region C (10°S–20°N, 125°–145°E).

Above all, the Niño-3.4 index is found to be highly correlated to TWI SST with the correlation coefficient being 0.5, so that statistical technique is of little value in discriminating the role of ENSO from TWI. To circumvent the problem, the LBM simulations are employed to study the effect of ENSO on SEMA precipitation. The three experimental runs are forced by El Niño, EP El Niño, and CP El Niño conditions, which are SST composites averaged for years with the corresponding indices above 0.8 standard deviations. The composite SST patterns are shown in the left column of Fig. S6, but note that only the anomalies in the tropical Pacific region (15°S–15°N, 120°E–80°W) are prescribed in the LBM boundary condition. The modeled responses are shown in the right column of Fig. S6, including low-level wind along with divergence at 900 hPa and vertical velocity at 500 hPa. As shown in Figs. S6b and S6d, the simulations show very similar patterns in El Niño and EP El Niño events, with an anticyclone formed in the South China Sea and Philippines as a consequence of the Gill mode response (Gill 1980). Associated with the anomalous anticyclone, southwesterlies on the western flank advect more moisture into the eastern coast of Indo-China Peninsula and southern China, leading to enhanced moisture convergence, ascents, and rainfall there. In terms of SEMA, significant anomalous conditions are confined to the eastern coastal areas. In contrast to EP El Niño, the CP El Niño anomalies are simply not strong enough to perturb the East Asia–northwestern Pacific atmospheric circulation, as reflected by Fig. S6f. The result is generally consistent with the recent work by Li et al. (2021). In brief summary, the Indian Ocean has more pronounced impact on SEMA than the remote influence from the Pacific Ocean.

Knowing the ENSO effect, the goal here moving forward will be to document the modulating role of ENSO on the decadal relation between TWI SST and SEMA precipitation. Above all, the temporal dispersions of two types of ENSO clustered for the six consecutive decades are shown in Fig. S7. It can be seen that during the 1980s to the 1990s the amplitude of EP El Niño is much stronger than that of the CP El Niño, whereas many of the El Niño events after 2000 appear as the CP type. This could explain why the dry period 1978–95 over SEMA features the westward shift of northeasterlies over SEMA and the intervention of the anticyclone sweeping the east flank of SEMA (Fig. 13d), in comparison to the recent decade.

The above studies were intended to determine the modulating effect of ENSO of concurrent spring, whereas the following work attempts to examine the indirect influence of ENSO in the preceding winter. Figure 14a shows the scatter and joint probability kernel density of TWI SST and SEMA

precipitation in spring across all years. It can be seen that the SEMA rainfall tends to decrease with respect to the increase of TWI SST. There is a negative correspondence between them, with the correlation coefficient being −0.23, which is significant at 0.1 level. However, the correlation score is not high, and we speculate that the effect of preceding winter ENSO may modulate the spring TWI SST and SEMA precipitation, because SST anomalies from ENSO tend to peak in winter. In view of the above, the interrelation between TWI SST and SEMA precipitation is conditioned on prior winter ENSO status, as shown in Figs. 14b and 14c for non-ENSO and ENSO phases, respectively. Figure 14b suggests that the SEMA precipitation is likely to be decoupled from the TWI SST under ENSO-neutral condition, since the correlation value is close to zero. In contrast, a tight linkage between TWI SST and SEMA precipitation is favored during the ENSO context, as the linear correlation indicated by Fig. 14c amounts to −0.46. A likely reason for this outcome is that following El Niño or La Niña mature winter, the Indian Ocean warming or cooling persists well into the subsequent spring through the tropospheric temperature mechanism and ocean dynamics (Zheng et al. 2011). However, there remains much to be learned about the role of ENSO background in fostering TWI SST and SEMA precipitation connection in the subsequent spring.

5. Conclusions

In the last decade (2010–19), southeastern mainland Asia (SEMA) has been in an extreme drought cycle. This study is thus motivated to inspect the decadal background and the underlying physical mechanism, based on both statistical diagnoses and numerical experiment.

During 2000–09, SEMA was less exposed to severe and extreme droughts. However, in the subsequent decade, severe drought conditions in the SEMA deteriorated drastically, with the regional average frequency having more than doubled. In particular, the 2010–19 episode is also identified as the period with the highest extent hit by severe or extreme droughts. By dividing the entire year into the four seasons, a concurrent transition in spring precipitation from a wet phase to a dry phase is found, with the turning point in 2010. Furthermore, such decadal shift can explain 43% of the regime shift toward more frequently extreme events in the recent decade.

The dynamic processes and key remote forcing underpinning the decadal precipitation change are schematically summarized in Fig. 15. On the one hand, the anomalous winds from northeasterlies to easterlies flow over the northern equatorial Indian Ocean, which hinders the moisture transport from the Indian Ocean. On the other hand, the convection in SEMA is suppressed in the presence of sinking motion, which is a manifestation of vertical circulation cell connecting rising motion over the TWI. Further investigation reveals that decadal SST variation in the TWI, negatively correlated with the SEMA precipitation, plays a substantial role in this climate shift. TWI SST changed from negative to positive around 2010, after which the persistent
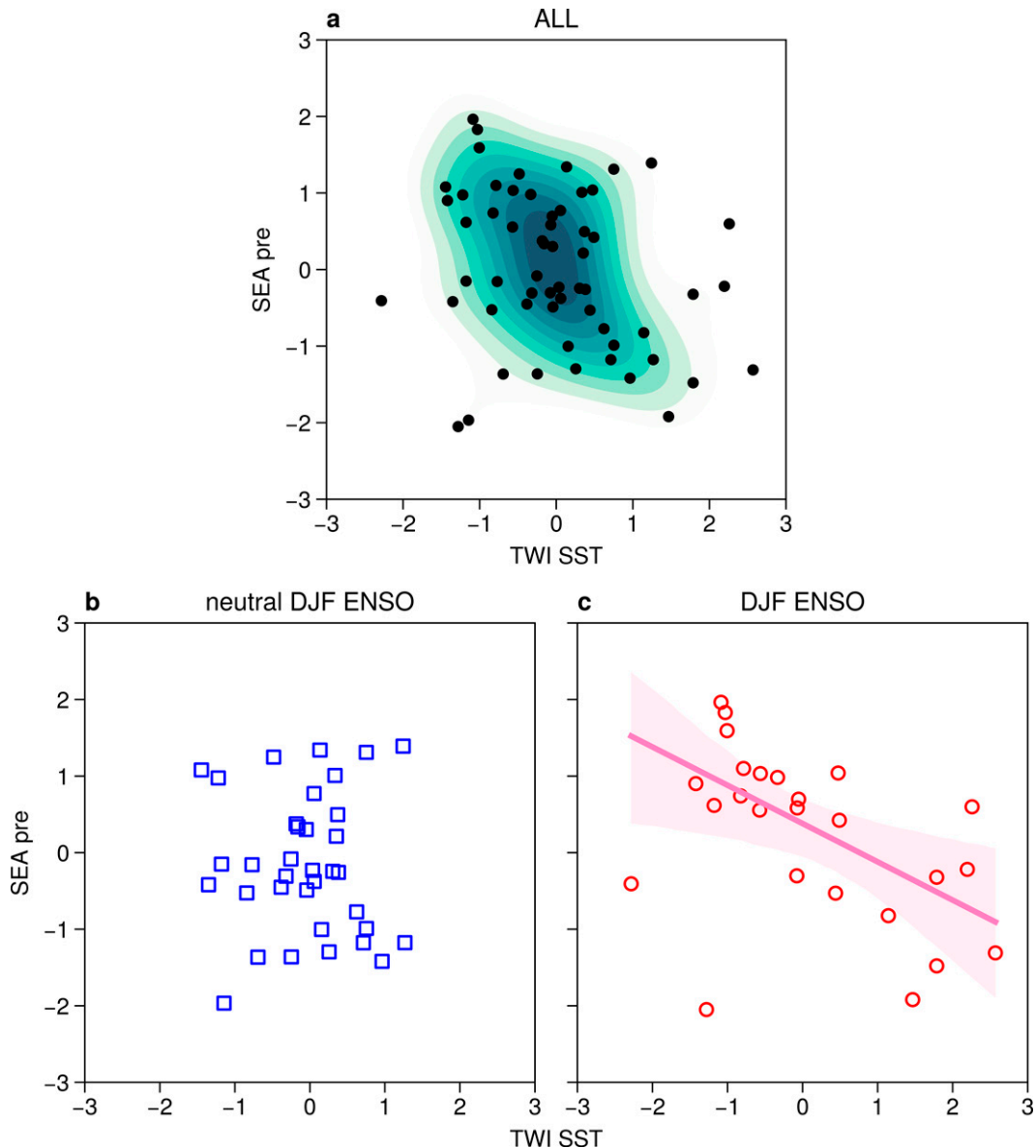
FIG. 14. (a) Scatterplot and joint probability kernel density of the normalized SEMA precipitation (*x* axis) vs TWI SST (*y* axis) during spring. (b),(c) As in (a), but separated into two groups: non-ENSO and ENSO years in the preceding winter, respectively. The ENSO event is identified according to when the absolute magnitude of the Niño-3.4 index is greater than or equal to 0.8 standard deviations. The linear regression line and 95% confidence interval are overlaid in (c).

warm SST served to maintain deficient SEMA precipitation in the recent decade. This decadal teleconnection occurs mainly through the Kelvin wave–induced low-level northwesterly and concordant downward motions in SEMA, as a consequence of heating in TWI. Further, the simulated structure forced by TWI SST alone bears a close resemblance to the observed evidence, confirming the critical role of the TWI. In addition, it is illustrated that ENSO and its diversity have modulating effects on SEMA precipitation as well as the coupling between TWI SST and SEMA

precipitation, during both the previous winter and the concurrent spring.

Finally, we would like stress that this study primarily examined the natural forcing in shaping the decadal background of regional extreme drought over SEMA. However, it should not be overlooked that the effects of anthropogenic forcing are growing as global warming continues. Recent advances by Song et al. (2018, 2021) have pointed out the delayed onset of tropical rainfall, with more evident manifestations over land (Song et al. 2020). The seasonal
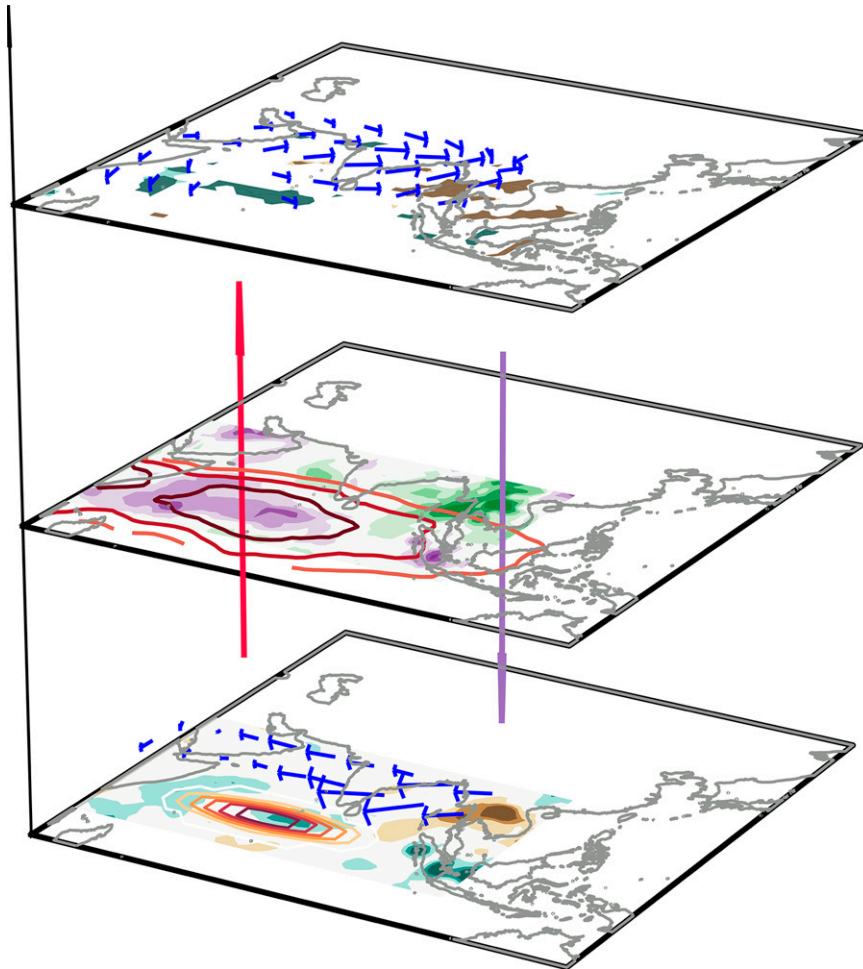
FIG. 15. Schematic diagram of the proposed mechanisms responsible for the active extreme drought over SEMA in the recent decade via TWI-related positive SST anomalies. (bottom) Shading, vectors, and contours denote anomalous moisture divergence, moisture flux, and TWI SST, respectively. (middle) Contours and shading indicate the anomalous 850–200-hPa temperature and vertical velocity, respectively. The vertical upward and downward arrows passing through the middle panel show the direction of vertical motion. (top) Vectors and shading represent the divergent wind and divergence anomalies, respectively.

delay is found to occur in response to elevated latent energy demand in the hemisphere warming up seasonally, most of which is driven by external forcing related to increasing greenhouse gases and anthropogenic aerosols. As greenhouse gases are expected to increase and aerosol forcing to decrease, the seasonal delay is projected to further amplify in the future. SEMA is certainly one of the regions affected by such a rule. Therefore, it can be preliminarily inferred that the joint effect of decadal variability and anthropogenic forcing may exacerbate the spring drought over SEMA in the coming decades. Future work should integrate the role of anthropogenic and natural effects in studying the extreme drought over SEMA.

Data availability statement. CRU TS4.04 precipitation and PET: http://data.ceda.ac.uk/badc/cru/data/cru_ts/cru_ts_4.04
ETOPO 1-arc-min gridded elevation: https://www.ngdc.noaa.gov/mgg/global/
GlobCover land Cover: http://due.esrin.esa.int/page_globcover.php
JRA-55: http://search.diasjp.net/en/dataset/JRA55
HadISST: https://www.metoffice.gov.uk/hadobs/hadisst/

REFERENCES

Amante, C., and B. W. Eakins, 2009: ETOPO1 1 Arc-Minute Global Relief Model: Procedures, data sources and analysis. NOAA Tech. Memo. NESDIS NGDC-24, 19 pp.

Ashok, K., S. K. Behera, S. A. Rao, H. Weng, and T. Yamagata, 2007: El Niño Modoki and its possible teleconnection. *J. Geophys. Res.*, **112**, C11007, https://doi.org/10.1029/2006JC003798.

Barriopedro, D., C. M. Gouveia, R. M. Trigo, and L. Wang, 2012: The 2009/10 drought in China: Possible causes and impacts on vegetation. *J. Hydrometeor.*, **13**, 1251–1267, https://doi.org/10.1175/JHM-D-11-074.1.

Christidis, N., K. Manomaiphiboon, A. Ciavarella, and P. A. Stott, 2018: The hot and dry April of 2016 in Thailand (in "Explaining Extreme Events of 2016 from a Climate Perspective"). *Bull. Amer. Meteor. Soc.*, **99**, S128–S132, https://doi.org/10.1175/BAMS-D-17-0071.1.

Ding, T., and H. Gao, 2020: The record-breaking extreme drought in Yunnan Province, Southwest China during spring–early summer of 2019 and possible causes. *J. Meteor. Res.*, **34**, 997–1012, https://doi.org/10.1007/s13351-020-0032-8.

Edwards, D. C., and T. B. McKee, 1997: Characteristics of 20th century drought in the United States at multiple time scales. Colorado State University, Atmospheric Science Paper 634, 155 pp.

ESCAP, 2019: *Ready for the Dry Years: Building Resilience to Drought in South-East Asia.* UN Economic and Social Commission for Asia and the Pacific, 126 pp., https://www.unescap.org/publications/ready-dry-years-building-resilience-drought-south-east-asia-2nd-edition.

Feng, J., W. Chen, C. Y. Tam, and W. Zhou, 2011: Different impacts of El Niño and El Niño Modoki on China rainfall in the decaying phases. *Int. J. Climatol.*, **31**, 2091–2101, https://doi.org/10.1002/joc.2217.

Frankignoul, C., G. Gastineau, and Y.-O. Kwon, 2017: Estimation of the SST response to anthropogenic and external forcing and its impact on the Atlantic multidecadal oscillation and the Pacific decadal oscillation. *J. Climate*, **30**, 9871–9895, https://doi.org/10.1175/JCLI-D-17-0009.1.

Gill, A. E., 1980: Some simple solutions for heat-induced tropical circulation. *Quart. J. Roy. Meteor. Soc.*, **106**, 447–462, https://doi.org/10.1002/qj.49710644905.

Harada, Y., and Coauthors, 2016: The JRA-55 reanalysis: Representation of atmospheric circulation and climate variability. *J. Meteor. Soc. Japan*, **94**, 269–302, https://doi.org/10.2151/jmsj.2016-015.

Harris, I., T. J. Osborn, P. Jones, and D. Lister, 2020: Version 4 of the CRU TS monthly high-resolution gridded multivariate climate dataset. *Sci. Data*, **7**, 109, https://doi.org/10.1038/s41597-020-0453-3.

Hayes, M., M. Svoboda, N. Wall, and M. Widhalm, 2011: The Lincoln declaration on drought indices: Universal meteorological drought index recommended. *Bull. Amer. Meteor. Soc.*, **92**, 485–488, https://doi.org/10.1175/2010BAMS3103.1.

Jia, X., Q. Gu, Q. Qian, and R. Wu, 2021: Wet-to-dry climate shift of the Sichuan Basin during 1961–2010. *Climate Dyn.*, **57**, 671–685, https://doi.org/10.1007/s00382-021-05734-8.

Kobayashi, S., and Coauthors, 2015: The JRA-55 Reanalysis: General specifications and basic characteristics. *J. Meteor. Soc. Japan*, **93**, 5–48, https://doi.org/10.2151/jmsj.2015-001.

Leung, M. Y.-T., W. Zhou, D. Wang, P. W. Chan, S. M. Lee, and H. W. Tong, 2020: Remote tropical western Indian Ocean forcing on changes in June precipitation in South China and the Indochina Peninsula. *J. Climate*, **33**, 7553–7566, https://doi.org/10.1175/JCLI-D-19-0626.1.

Li, R. K. K., C. Y. Tam, and N. C. Lau, 2021: Effects of ENSO diversity and cold tongue bias on seasonal prediction of South China late spring rainfall. *Climate Dyn.*, **57**, 577–591, https://doi.org/10.1007/s00382-021-05732-w.

Ma, T., W. Chen, H.-F. Graf, S. Ding, P. Xu, L. Song, and X. Lan, 2020: Different impacts of the East Asian winter monsoon on the surface air temperature in North America during ENSO and neutral ENSO years. *J. Climate*, **33**, 10671–10690, https://doi.org/10.1175/JCLI-D-18-0760.1.

McKee, T. B., N. J. Doesken, and J. Kleist, 1993: The relationship of drought frequency and duration to time scales. Preprints, *Eighth Conf. on Applied Climatology*, Anaheim, CA, Amer. Meteor. Soc., 179–184.

Nguyen-Ngoc-Bich, P., and Coauthors, 2021: Projected evolution of drought characteristics in Vietnam based on CORDEX-SEA downscaled CMIP5 data. *Int. J. Climatol.*, **41**, 5733–5751, https://doi.org/10.1002/joc.7150.

Park, C.-K., D.-S. R. Park, C.-H. Ho, T.-W. Park, J. Kim, S. Jeong, and B.-M. Kim, 2020: A dipole mode of spring precipitation between Southern China and Southeast Asia associated with the eastern and central Pacific types of ENSO. *J. Climate*, **33**, 10097–10111, https://doi.org/10.1175/JCLI-D-19-0625.1.

Qian, Q. F., R. Wu, and X. J. Jia, 2020: Persistence and nonpersistence of East and Southeast Asian rainfall anomaly pattern from spring to summer. *J. Geophys. Res. Atmos.*, **125**, e2020JD033404, https://doi.org/10.1029/2020JD033404.

Rayner, N. A., D. E. Parker, E. B. Horton, C. K. Folland, L. V. Alexander, D. P. Rowell, E. C. Kent, and A. Kaplan, 2003: Global analyses of sea surface temperature, sea ice, and night marine air temperature since the late nineteenth century. *J. Geophys. Res.*, **108**, 4407, https://doi.org/10.1029/2002JD002670.

ReliefWeb, 2017: South-East Asia: Drought—2015–2017. ReliefWeb, accessed 28 Mar 2022, https://reliefweb.int/disaster/dr-2015-000180-vnm.

——, 2020: Drought—2019–2020. ReliefWeb, accessed 28 Mar 2022, https://reliefweb.int/disaster/dr-2019-000113-phl.

Song, F., L. R. Leung, J. Lu, and L. Dong, 2018: Seasonally dependent responses of subtropical highs and tropical rainfall to anthropogenic warming. *Nat. Climate Change*, **8**, 787–792, https://doi.org/10.1038/s41558-018-0244-4.

——, J. Lu, L. R. Leung, F. Liu, 2020: Contrasting phase changes of precipitation annual cycle between land and ocean under global warming. *Geophys. Res. Lett.*, **47**, e2020GL090327, https://doi.org/10.1029/2020GL090327.

——, L. R. Leung, J. Lu, L. Dong, W. Zhou, B. Harrop, and Y. Qian, 2021: Emergence of seasonal delay of tropical rainfall during 1979–2019. *Nat. Climate Change*, **11**, 605–612, https://doi.org/10.1038/s41558-021-01066-x.

Sun, S., and Coauthors, 2019: Revisiting the evolution of the 2009–2011 meteorological drought over Southwest China. *J. Hydrol.*, **568**, 385–402, https://doi.org/10.1016/j.jhydrol.2018.10.071.

Supari, and Coauthors, 2020: Multi-model projections of precipitation extremes in Southeast Asia based on CORDEX-Southeast Asia simulations. *Environ. Res.*, **184**, 109350, https://doi.org/10.1016/j.envres.2020.109350.

Tan, H., R. Cai, J. Chen, and R. Huang, 2017: Decadal winter drought in Southwest China since the late 1990s and its

atmospheric teleconnection. *Int. J. Climatol.*, **37**, 455–467, https://doi.org/10.1002/joc.4718.

Tangang, F., and Coauthors, 2020: Projected future changes in rainfall in Southeast Asia based on CORDEX–SEA multi-model simulations. *Climate Dyn.*, **55**, 1247–1267, https://doi.org/10.1007/s00382-020-05322-2.

Thirumalai, K., P. N. DiNezio, Y. Okumura, and C. Deser, 2017: Extreme temperatures in Southeast Asia caused by El Niño and worsened by global warming. *Nat. Commun.*, **8**, 15531, https://doi.org/10.1038/ncomms15531.

Torres, M. E., M. A. Colominas, G. Schlotthauer, and P. Flandrin, Eds., 2011: A complete ensemble empirical mode decomposition with adaptive noise. *2011 IEEE Int. Conf. on Acoustics, Speech and Signal Processing (ICASSP)*, Prague, Czech Republic, Institute of Electrical and Electronics Engineers, 4144–4147.

Vicente-Serrano, S. M., S. Beguería, and J. I. López-Moreno, 2010: A multiscalar drought index sensitive to global warming: The standardized precipitation evapotranspiration index. *J. Climate*, **23**, 1696–1718, https://doi.org/10.1175/2009JCLI2909.1.

Wang, L., and W. Chen, 2014: A CMIP5 multimodel projection of future temperature, precipitation, and climatological drought in China. *Int. J. Climatol.*, **34**, 2059–2078, https://doi.org/10.1002/joc.3822.

——, ——, and W. Zhou, 2014: Assessment of future drought in Southwest China based on CMIP5 multimodel projections. *Adv. Atmos. Sci.*, **31**, 1035–1050, https://doi.org/10.1007/s00376-014-3223-3.

——, ——, ——, and G. Huang, 2015: Drought in Southwest China: A review. *Atmos. Oceanic Sci. Lett.*, **8**, 339–344, https://doi.org/10.3878/AOSL20150043.

——, G. Huang, W. Chen, W. Zhou, and W. Wang, 2018: Wet-to-dry shift over Southwest China in 1994 tied to the warming of tropical warm pool. *Climate Dyn.*, **51**, 3111–3123, https://doi.org/10.1007/s00382-018-4068-8.

——, W. Chen, Q. Fu, G. Huang, Q. Wang, C. Chotamonsak, A. Limsakul, 2021: Super droughts over East Asia since 1960 under the impacts of global warming and decadal variability. *Int. J. Climatol.*, in press, https://doi.org/10.1002/joc.7483.

Wang, S., J. Huang, and X. Yuan, 2021: Attribution of 2019 extreme spring–early summer hot drought over Yunnan in Southwestern China. *Bull. Amer. Meteor. Soc.*, **102** (1), S91–S96, https://doi.org/10.1175/BAMS-D-20-0121.1.

Watanabe, M., 2003: Linear Baroclinic Model (LBM) Package Users' Guide, https://ccsr.aori.u-tokyo.ac.jp/~lbm/sub/lbm.html.

——, and F.-F. Jin, 2003: A moist linear baroclinic model: Coupled dynamical–convective response to El Niño. *J. Climate*, **16**, 1121–1139, https://doi.org/10.1175/1520-0442(2003)16<1121:AMLBMC>2.0.CO;2.

Wu, B., T. Zhou, and T. Li, 2009: Seasonally evolving dominant interannual variability modes of East Asian climate. *J. Climate*, **22**, 2992–3005, https://doi.org/10.1175/2008JCLI2710.1.

Xie, S.-P., K. Hu, J. Hafner, H. Tokinaga, Y. Du, G. Huang, and T. Sampe, 2009: Indian Ocean capacitor effect on Indo-western Pacific climate during the summer following El Niño. *J. Climate*, **22**, 730–747, https://doi.org/10.1175/2008JCLI2544.1.

Yang, J., D. Gong, W. Wang, M. Hu, and R. Mao, 2012: Extreme drought event of 2009/2010 over southwestern China. *Meteor. Atmos. Phys.*, **115**, 173–184, https://doi.org/10.1007/s00703-011-0172-6.

Zhang, L., Z. Chen, and T. Zhou, 2021: Human influence on the increasing drought risk over Southeast Asian monsoon region. *Geophys. Res. Lett.*, **48**, e2021GL093777, https://doi.org/10.1029/2021GL093777.

Zhang, W., F.-F. Jin, J.-X. Zhao, L. Qi, and H.-L. Ren, 2013: The possible influence of a nonconventional El Niño on the severe autumn drought of 2009 in Southwest China. *J. Climate*, **26**, 8392–8405, https://doi.org/10.1175/JCLI-D-12-00851.1.

Zheng, X.-T., S.-P. Xie, and Q. Liu, 2011: Response of the Indian Ocean basin mode and its capacitor effect to global warming. *J. Climate*, **24**, 6146–6164, https://doi.org/10.1175/2011JCLI4169.1.